Research Article | Vol. 29, No. 17 / 16 August 2021 / Optics Express 26353
Optics EXPRESS

Strain-, curvature- and twist-independent temperature sensor based on a small air core hollow core fiber structure

DEJUN LIU,[1,7] WEI LI,[1,7] QIANG WU,[2,3] FENGZI LING,[1] KE TIAN,[4] CHANGYU SHEN,[5] FANGFANG WEI,[6] GERALD FARRELL,[6] YULIYA SEMENOVA,[6] AND PENGFEI WANG[1,4,*]

[1]*Key Laboratory of Optoelectronic Devices and Systems of Ministry of Education and Guangdong Province, College of Physics and Optoelectronic Engineering, Shenzhen University, Shenzhen 518060, China*
[2]*Key Laboratory of Nondestructive Test (Ministry of Education), Nanchang Hangkong University, Nanchang 330063, China*
[3]*Department of Mathematics, Physics and Electrical Engineering, Northumbria University, Newcastle Upon Tyne NE1 8ST, United Kingdom*
[4]*Key Lab of In-fiber Integrated Optics, Ministry Education of China, Harbin Engineering University, Harbin 150001, China*
[5]*Institute of Optoelectronic Technology, China Jiliang University, Hangzhou 310018, China*
[6]*Photonics Research Centre, Technological University Dublin, Kevin Street, Dublin 8, Ireland*
[7]*These authors contribute equally*
[*]*pfwang@szu.edu.cn*

Abstract: Cross-sensitivity (crosstalk) to multiple parameters is a serious but common issue for most sensors and can significantly decrease the usefulness and detection accuracy of sensors. In this work, a high sensitivity temperature sensor based on a small air core (10 μm) hollow core fiber (SACHCF) structure is proposed. Co-excitation of both anti-resonant reflecting optical waveguide (ARROW) and Mach-Zehnder interferometer (MZI) guiding mechanisms in transmission are demonstrated. It is found that the strain sensitivity of the proposed SACHCF structure is decreased over one order of magnitude when a double phase condition (destructive condition of MZI and resonant condition of ARROW) is satisfied. In addition, due to its compact size and a symmetrical configuration, the SACHCF structure shows ultra-low sensitivity to curvature and twist. Experimentally, a high temperature sensitivity of 31.6 pm/°C, an ultra-low strain sensitivity of −0.01pm/με, a curvature sensitivity of 18.25 pm/m^{-1}, and a twist sensitivity of −22.55 pm/(rad/m) were demonstrated. The corresponding temperature cross sensitivities to strain, curvature and twist are calculated to be −0.00032 °C/με, 0.58 °C/m^{-1} and 0.71 °C/(rad/m), respectively. The above cross sensitivities are one to two orders of magnitude lower than that of previously reported optical fiber temperature sensors. The proposed sensor shows a great potential to be used as a temperature sensor in practical applications where influence of multiple environmental parameters cannot be eliminated.

1. Introduction

Optical fiber sensors (OFSs) have attracted tremendous interest for the detection of changes in physical and bio-chemical parameters in a variety of applications due to their inherent advantages such as high sensitivity, compact size, fast response, good resistance to electromagnetic interference, and capability to work in harsh environments [1]. At present the range and complexity of the application areas for optical fiber sensors has been rising and cross-sensitivity to multiple parameters has become an increasingly important issue since it can render some sensors unusable in some cases or can significantly decrease the detection accuracy of a sensor. There is thus a strong demand for sensors with high sensitivity to the target parameters, but low cross-sensitivity

#433580 https://doi.org/10.1364/OE.433580
Journal © 2021 Received 8 Jun 2021; revised 17 Jul 2021; accepted 23 Jul 2021; published 2 Aug 2021

Optics EXPRESS

to other ambient parameters. In the past decades, a lot of effort have been invested in developing optical fiber sensors to address the issue of cross-sensitivity by employing customized fiber sensor structures and hybrid structures which provide compensation techniques [2–9].

Temperature is one of the key measurement parameters that is most frequently encountered in a wide range of applications from civil engineering, petrochemical industries, bioengineering to mechanical engineering [1]. In many temperature measurement environments, there is also the presence of unavoidable strain, curvature/bending and twist/torsion effects. For example in civil engineering structures, as temperature changes, thermal expansion of structural elements can occur which in a structure can result in a change in strain or bending, which in turn can be detected by an attached temperature sensor which has a cross sensitivity to strain or bending. A number of fiber structures have been proposed for temperature measurement such as fiber Bragg gratings (FBGs) [10–11], Fabry-Perot interferometers (FPIs) [12–13], Mach–Zehnder interferometers (MZIs) [3–7], and Sagnac interferometers [14–15]. A good example is a MZI which provides simple fabrication and high sensitivity when used as a temperature sensor, but it suffers from high cross sensitivities to strain, curvature/bending and twist/torsion. Recently, a few MZIs have been proposed for strain independent temperature measurement based on modified singlemode-multimode-singlemode (SMS) structures by using a seven-core fiber, a suspended-core fiber, a small core photosensitive fiber, multiple sections of singlemode and multimode fibers, and a photonic crystal fiber [3–7], but these fiber structures are demonstrated with high cross sensitivity to curvature [16–19]. To date, there has been no temperature sensors proposed with a high resistance to all above three parameters (strain, curvature and twist).

Recently, hollow core fiber (HCF) and functionalized HCF which guide light through Anti-Resonant Reflecting Optical Waveguide (ARROW) effect have been intensively investigated as a temperature and strain sensor [20–21], a curvature sensor [22], and a twist sensor [23]. Most recently, excitation of multiple light guiding mechanisms in HCF has been increasingly popular in sensing of multiple parameters and various sensor structures have been proposed. For example, Gao *et al.* proposed a self-temperature-calibrated gas pressure sensor by sandwiching a short section of HCF between two SMFs to form a SMF-HCF-SMF (SHS) structure, both FPI and ARROW guiding mechanisms are demonstrated in reflection [24]. Ni *et al.* reports the excitation of ARROW and MZI guiding mechanisms using a single hole twin eccentric core fiber, simultaneous measurement of curvature and temperature was realized by tracking the power and wavelength shift of the resonant dip [25]; Zuo *et al.* incorporated two sections of multimode fibers (MMFs) into SHS structure to produce a SMF-MMF-HCF-MMF-SMF (SMHMS) structure, both ARROW and MZI guiding mechanisms were excited within the sensor structure and simultaneous measurement of temperature and strain was experimentally achieved [26]. Cheng *et al.* proposed a hybrid fiber structure by fabricating two up-tapers at the splicing points between SMFs and HCF in the SHS structure to excite ARROW and MZI guiding mechanisms, the cross sensitivity between temperature and curvature can be distinguished by tracking the wavelength shift of MZI dip and intensity variation of ARROW dip [27]. It is noted that most of the reports on SHS structure to date are based on a big air core (usually bigger than 20 μm) HCF (BACHCF) structure where only ARROW guiding mechanism is excited. To introduce other light transmission mechanism, for example MZI, traditional SHS structure needs to be modified. However modification of SHS structure is usually complex and may decrease its reproducibility. For example, the shape of up-taper is usually difficult to control due to the variations in arc power and arc position, which could introduce a significant change in mode coupling from SMF to HCF.

By varying both the air core diameter of HCF and fusion splicing power between SMF and HCF, different light guiding mechanisms can be excited within the SHS structure [28], and accordingly its sensing properties can be tuned further. In this paper, co-excitation of both ARROW and MZI guiding mechanisms in SHS structure is realized by employing a small air core

Optics EXPRESS

(10 μm) HCF (SACHCF). Compared to above mentioned single hole twin eccentric core fiber structure, SMHMS structure and SHS structure combined with two up-tapers, the SACHCF based SHS structure is much more compact and easier in fabrication. It is found that the wavelength shifts of the dips produced by ARROW and MZI guiding mechanisms differ in sign when strain is applied. When a double phase matching condition (destructive condition of MZI and resonant condition of ARROW) is satisfied in the proposed SACHCF structure, dips produced by two mechanisms overlap, the overlapped dip shows a 50 times lower strain sensitivity of −0.01 pm/με while its temperature sensitivity around room temperature (31.6 pm/°C) is nearly doubled compared to that of a BACHCF structure [20–21]. Due to its compact size and a symmetrical configuration, the SACHCF structure also shows ultra-low sensitivities to curvature and twist. In addition, the sensor could work in a wide measurement range, the sensor head has a length of only a few hundreds of microns, it offers the potential of higher spatial resolution for temperature measurement.

2. Experimental setup

Experimentally, an SACHCF (Fiberguide Industries CAP010/150/24 T) with an inner air core diameter of 10 μm and outer cladding diameter of 126 μm was used. The proposed sensor structure was fabricated by fusion splicing a short section of an SACHCF between two singlemode fibers (SMFs). The splicing power and time were carefully controlled to avoid collapse of the air core. Figures 1(a) and (b) show a schematic diagram of the proposed SACHCF structure and two optical microscope images of the prepared sensor samples with HCF lengths of 707 μm and 866 μm, denoted hereafter as S-707 and S-866, respectively. Light transmission within such an SACHCF is illustrated with arrows in Fig. 1(a) where the blue and red arrows indicate different light guiding principles of ARROW and MZI, respectively. The experimental setup for the measurement of temperature, stain, curvature and torsion is shown in Fig. 1(c). The fiber structure was fixed in a straight line on a manual translation stage and a fiber rotator. The strain and curvature measurements were realized by moving the translation stage in opposite directions. Curvature calculation is based on the following equation [29]:

$$C = \sqrt{\frac{24x}{(L_0 - x)^3}} \tag{1}$$

where x is moved distance of the translation stage, L_0 is the initial distance between the two moving stages. The twist measurement was achieved with a fiber rotator and the temperature test was carried out by placing the sensor structure on a hot plate. Light from a broadband supercontinuum source (SC-YSL) (SC) was launched into the SACHCF based structure and the transmitted light was interrogated by an OSA (Yokogawa AQ6370D).

The light guiding mechanism in an HCF structure can be analyzed using the ARROW model where light is confined and transmitted inside the air core when the anti-resonance condition is satisfied in the silica cladding [24]. If the resonance condition is satisfied, light will leak into the surrounding environment, producing periodic dips in the transmission response. The resonant wavelength (λ_m^{AR}) and the corresponding free spectral range (FSR) between two adjacent resonant dips (FSR_{AR}) can be predicted with the following equations [30]:

$$\lambda_m^{AR} = \frac{2t}{m}\sqrt{n_1^2 - n_0^2} \tag{2}$$

$$FSR_{AR} = \frac{\lambda_m \lambda_{m+1}}{2t\sqrt{n_1^2 - n_0^2}} \tag{3}$$

Optics EXPRESS

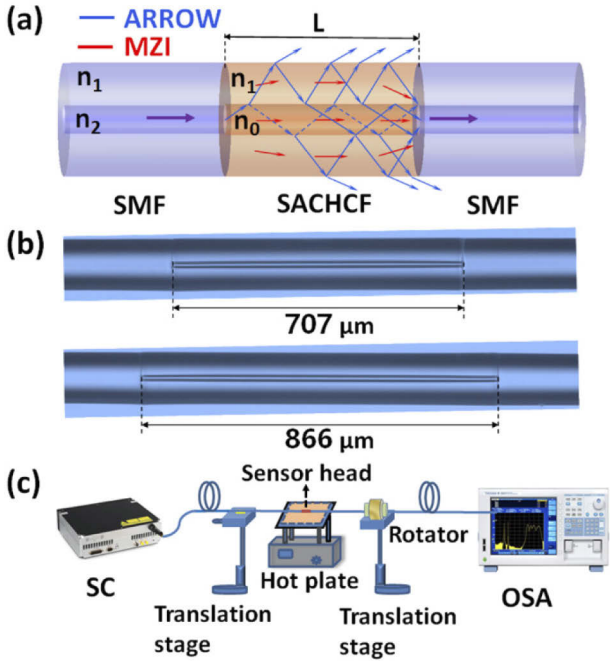

Fig. 1. (a) A schematic diagram and (b) optical microscope images of the proposed SACHCF structure; (c) experimental setup for measurements of multiple parameters.

where n_1 and n_0 are the refractive indices of the silica cladding and air core of the HCF, t is the thickness of the silica cladding and m is the resonance order (m is a nonnegative integer). In this work, n_1 and n_0 are assumed to be 1.45 and 1.0 respectively.

An MZI guiding mechanism is excited when the core diameters of the HCF and the SMF are comparable in magnitude [31]. For a typical SMF, the mode field diameter (MFD) of the fundamental modal is around 10.4 μm [31]. When the MFD is bigger than the air core diameter of the HCF, a portion of the light from the SMF propagates in the air core of the SACHCF while the remaining portion of light is coupled into the silica cladding. These two distinct light portions recombine and interfere with each other at the end of the SACHCF at the output SACHCF-SMF interface, so that the structure forms an MZI. The operation of this MZI can be explained with a "two-beam optical interference model", where the resonant dips (λ_m^{MZ}) and the corresponding FSR between any two adjacent dips in the transmission spectrum can be derived as [32]:

$$\lambda_m^{MZ} = 2\triangle n_{eff} L/(2m+1) \tag{4}$$

$$FSR_{MZI} = \frac{\lambda_m \lambda_{m+1}}{\triangle n_{eff} L} \tag{5}$$

where Δn_{eff} is the difference between the effective refractive indices of the two interfering modes and L is the interference length which is the length of SACHCF section, in effect the sensor head in this structure.

3. Results and discussion

To investigate the light guiding mechanism, sensor samples with HCF lengths of 707 μm and 866 μm were placed in air and in water, respectively, their transmission spectra were recorded and the results are shown in Fig. 2. Strong periodic dips with small variations in their central

Optics EXPRESS

wavelengths (less than 0.5 nm) are excited in air for both samples with a FSR of circa 21 nm at 1570 nm. Clearly these strong dips are produced by the ARROW effect as the dip wavelengths are independent of the sensor length and the fact that the measured FSR is well matched with the theoretical value (20.3 nm) calculated by Eq. (3).

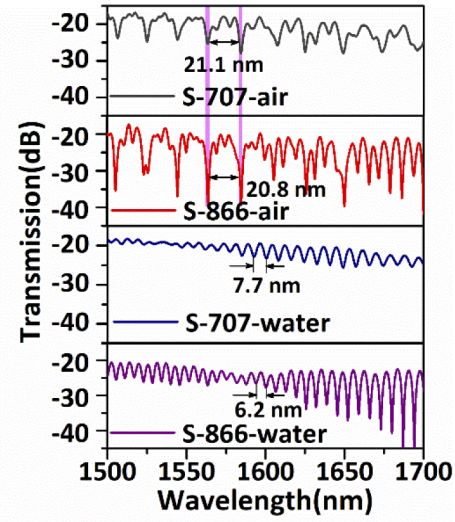

Fig. 2. Measured transmission spectra of S-707 and S-866 in air and water.

Some small spectral ripples are also present in the transmission spectra in air. To identify the origin of these small ripples, the sensor heads of both samples were immersed in water. Since it is known that the ARROW dips are significantly reduced in water [33], the spectral dips that remain in water can only be caused by the MZI effect. Experimentally as expected, the strong dips disappear in water while the small ripples remain. These ripples have a lower FSR value which decreases with an increase in the HCF length. The sensor samples S-707 and S-866 have FSR values of 7.7 nm and 6.2 nm at 1600 nm respectively, which matches well with the theoretically calculated values of 8.0 nm and 6.6 nm using Eq. (5). Note that the strength of MZI dips increases with the length of HCF section, but the superposition of the multiple ARROW dips and MZI dips increases the difficulty in distinguishing between different types of transmission dips for a longer HCF sample.

Figure 3 shows the fast Fourier transform (FFT) spatial frequency spectra corresponding to the measured transmission spectra in Fig. 2. A number of major spatial frequency peaks (labelled A1, A2, A3, A4; B1, B2, B3, B4; C1, C2; D1, D2) were observed, which indicates that multiple modes are involved in the interference fringe patterns. It can be seen that frequencies A1 and B1 are the dominant frequencies for both samples with an almost equal value of frequency, which confirms that they originate from the ARROW effect since the ARROW-induced resonant dip frequencies are independent on the length of the HCF. Dips at frequencies A1 and B1 disappear in water, hence ARROW dips are not observed in these transmission spectra. Dips at frequencies C1 and C2 shift to higher frequencies (D1 and D2) with the increase of HCF length, which is consistent with the behavior of MZI dips [34]. All the above evidence leads to the conclusion that both ARROW and MZI guiding mechanisms are simultaneously excited in such a SACHCF structure. It is noted that in addition to frequency A1, some other frequencies disappear in water, these frequencies are related to transmission ripples which could be attributed to the non-uniformity of the ring cladding thickness or some inter-mode interferences [35–36].

Optics EXPRESS

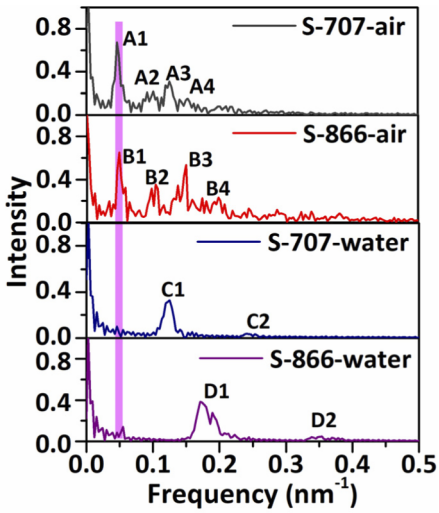

Fig. 3. FFT spatial frequency spectra corresponding to the transmission spectra shown in Fig. 2.

As can be seen in Fig. 2, there are a large number of transmission dips in the measurement range from 1500 nm to 1700 nm. It is necessary to determine which dips are the most appropriate to sense temperature, while demonstrating insensitivity to other environmental parameters. For this purpose the sensors' responses to a large applied strain were first measured. The spectral responses to strain are very complex, as shown in Fig. 4, where some of the dips shift to a shorter wavelength while some others move to a longer wavelength with an increase in strain, for example the dips at 1544.6 nm and at 1615.8 nm for S-707 and the dips at 1584.8 nm and 1611.2 nm for S-866. The wavelength regions for these dips are indicated by dashed black rectangles in Fig. 4. There are also some dips in Fig. 4 (indicated by pink shading) which have no obvious wavelength shift but which show intensity changes for both samples under a wide range of strain variations from 0 to 3000 με. These dips are suitable for strain independent temperature measurement, and further investigations on their sensing performances to curvature and twist were thus carried out as discussed below.

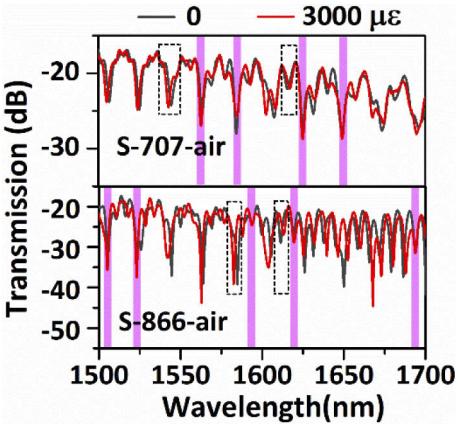

Fig. 4. Measured transmission spectra of S-707 and S-866 under different strains of 0 and 3000 με.

Optics EXPRESS

Figures 5 and 6 show examples of the measured transmission spectral responses of S-707 and S-866 subjected to changes in strain, temperature, curvature and twist. There are four major dips in the measurement range, which are denoted with the numbers 1, 2, 3, 4 and 1', 2', 3', 4' for sensors S-707 and S-866 respectively. It can be seen that all dips experience red shifts with an increase in temperature for both samples. In contrast, the spectral response to strain is much more complex where dip 2 is split into two dips with the increase of strain while a reverse transformation occurs for dips 2' and 3'. Dip 4' has the largest wavelength shift among all dips whilst other dips for both samples have very small wavelength shifts with variations in the applied strain. All dips show no obvious wavelength shift but intensity changes under the influence of bending (curvature) and twist. In order to better demonstrate the dip shifts, Figs. 7 and 8 show the magnified spectral changes of dips 1 and 1' for sensors S-707 and S-866 respectively. These two dips were selected because they have the best sensing performance among all dips, showing high temperature sensitivities but most importantly ultra-low cross sensitivities to strain, curvature and twist. (As will be demonstrated in comparison with other authors' work in Tables 1 and 2 to be discussed later in this paper).

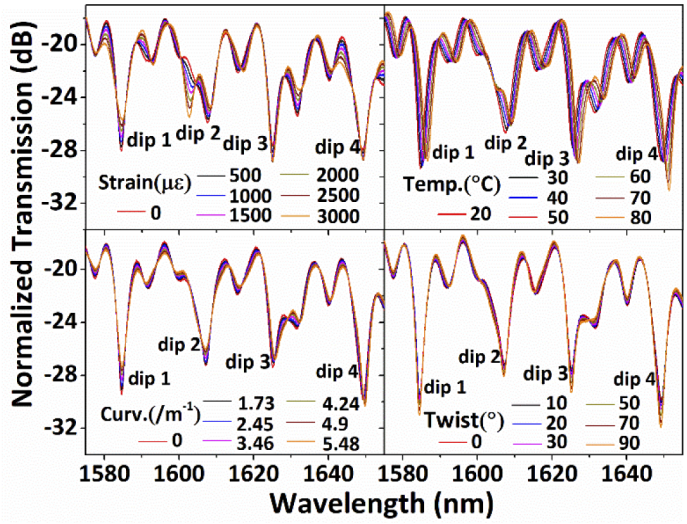

Fig. 5. Measured transmission spectral responses of S-707 under different strains, temperatures, curvatures and twist angles.

Figure 9(a) and (b) plot the wavelength shifts versus multiple parameters variations for dips 1 of S-707 and 1' of S-866, respectively. Both dips display linear wavelength shifts with temperature increase. When strain, curvature and twist were applied, both dips remained almost fixed with very tiny wavelength variations. In this work, the sensitivity of a dip is defined as:

$$S = \frac{\partial \lambda}{\partial P} \tag{6}$$

where λ is the dip wavelength and P is one of the environmental variables under test, for example, temperature. If the measured wavelength shift changes linearly with variations of tested environmental parameters, the sensitivity can be obtained from the slope of the linearly fitted curve. However some of the dips have little variations with the change of parameters, those little variations are poorly linearly fitted and hence the standard deviation (Std) of the measured data is calculated. Since the Std is very small (less than 100 pm) for all parameters tested, $\partial\lambda$ in Eq. (6) could be approximated with two times of Std during the test. In this work, we define a positive

Optics EXPRESS

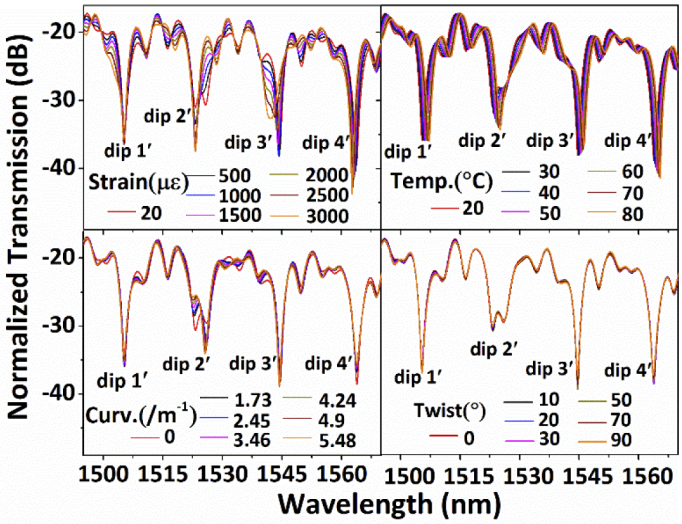

Fig. 6. Measured transmission spectral responses of S-866 under different strains, temperatures, curvatures and twist angles.

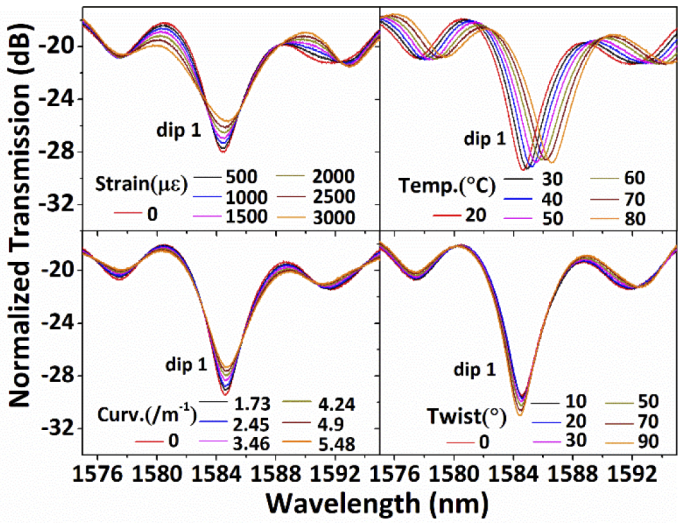

Fig. 7. Magnified transmission spectral responses of dip 1 of S-707 under different strains, temperatures, curvatures and twist angles.

Optics EXPRESS

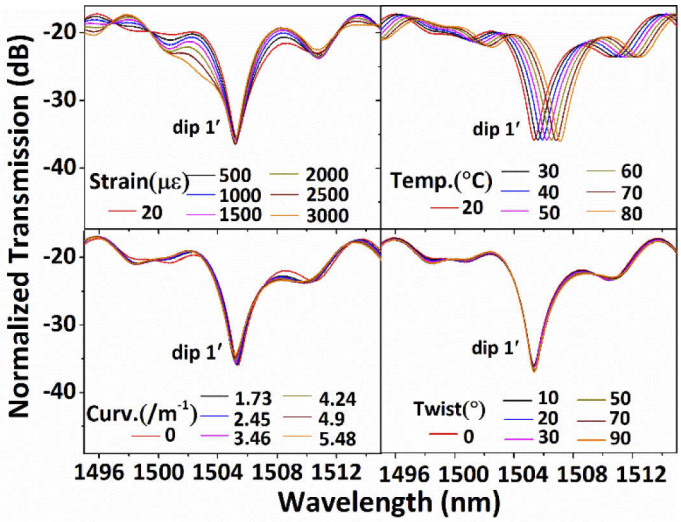

Fig. 8. Magnified transmission spectral responses of dip 1' of S-866 under different strains, temperatures, curvatures and twist angles.

Table 1. Selected dips' sensitivities to multiple parameters and their linear fit correlative coefficients (R^2). R^2 is replaced with the standard deviation (Std) of the measured data when the coefficient is less than 0.8.

Sensors	S-707		S-866	
	Dip **1**	Dip **4**	Dip **1'**	Dip **4'**
Temperature (pm/°C)	31.6	34.9	29.9	26.6
R^2	0.9977	0.9979	0.9986	0.9990
Strain (pm/με)	−0.01	0.06	−0.06	−0.38
R^2/Std(pm)	13	90	0.9777	0.9988
Curvature (pm/m^{-1})	18.25	111	−24.09	−13.87
R^2/Std(pm)	50	0.9791	66	38
Torsion (pm/(rad/m))	−22.55	−13.38	6.50	−14.9
R^2/Std(pm)	59	35	17	39

Table 2. Sensing performance of the proposed SACHCF structure in comparison with other fiber based temperature sensors.

Sensors	Temperature (pm/°C)	Strain (pm/με)	Curvature (pm/m^{-1})	Torision (pm/(rad/m))	Ref.
SMF-MMF-SMF	11.16	0.35-0.8	310-10380	/	39,40
SMF-Seven core fiber-SMF	123	1.02	3000	−400	3,16
SMF-Suspended-core fiber-SMF	25	0.08	/	/	6
SMF-MMF-SMF-MMF-SMF	50.65	0.587	14400	/	4,17
SMF-FBG-SMF	10	1.2	/	/	37
Fabry-Perot interferometer	1.3	5.2	/	/	41
SMF-PCF-SMF	73	0.93	4451	/	7,19
Sagnac Interferometer	0.93	21	/	/	42
SMF-SACHCF-SMF (dip1)	**31.6**	**−0.01**	**18.25**	**−22.55**	**This work**

Optics EXPRESS

sensitivity as that corresponding to a red wavelength shift while a negative sensitivity is related to a blue wavelength shift.

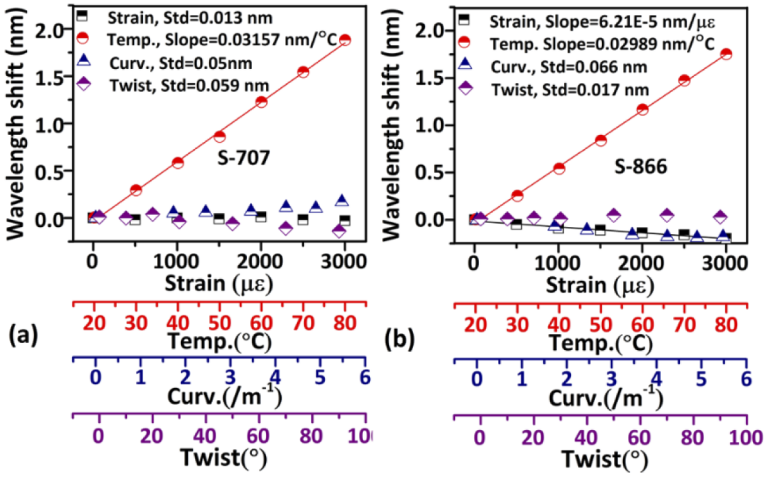

Fig. 9. Measured wavelength shifts with temperature, strain, curvature and twist angle changes for (a) dip 1 of S-707, and (b) dip 1' of S-866.

Table 1 summarizes some examples of the sensitivities of dips 1 and 4 of S-707 and dips 1' and 4' of S-866 to strain (0-3000 με), temperature (20-80 °C), curvature (0-6 /m^{-1}) and twist (0-90°). As one can see, dip 4 has the best sensitivity of 34.9 pm/°C to temperature. All dips and peaks show low sensitivity to strain, bending and twist. In particular, dip 1 has the lowest strain sensitivity of −0.01 pm/με, dip 1' has the lowest twist sensitivity of 6.5 pm/(rad/m) and dip 4' shows the lowest curvature sensitivity of −13.87 pm/m^{-1}. To further demonstrate the usefulness of the SACHCF structure and its more universal sensing properties, dip 4' which shows relatively large strain sensitivity was also selected to test its sensing performance to all four parameters in detail. Clearly it shows ultra-low cross-sensitivities to curvature and twist. However, the relatively large strain sensitivity of 0.38 pm/με is still low compared to other fiber sensors, for example, it constitutes only about one third of that for a typical FBG strain sensor [37].

The cross-sensitivity of a temperature sensor to strain, curvature or twist is defined as:

$$S_C = \frac{S_P}{S_T} \tag{7}$$

where S_T is the sensitivity to temperature, S_P is the sensitivity to other involved parameters (strain, curvature, or twist). Using this definition, the cross-sensitivities of dip 1 for example are −0.00032 °C/με, 0.58 °C/m^{-1} and 0.71 °C/(rad/m). Considering that 1 pm is the highest measurement resolution that could be achieved with a typical OSA, the cross-sensitivity to curvature, twist and moderate strain can be ignored during the temperature test when using the sensor proposed in this work.

The complex sensing performances of the different dips can be explained as follows. Based on Eqs. (2) and (4), the spectral wavelength shift of the ARROW and MZI dips subjected to temperature and strain variations can be derived using the following equations:

$$\frac{\partial \lambda_{dip}^{AR}}{\partial T} = \left[\frac{1}{t}\frac{\partial t}{\partial T} + \frac{n_1}{n_1^2 - 1}\frac{\partial n_1}{\partial T}\right]\lambda_{dip}^{AR} \tag{8}$$

$$\frac{\partial \lambda_{dip}^{AR}}{\partial \varepsilon} = \left[\frac{1}{t}\frac{\partial t}{\partial \varepsilon} + \frac{n_1}{n_1^2 - 1}\frac{\partial n_1}{\partial \varepsilon}\right]\lambda_{dip}^{AR} \tag{9}$$

Optics EXPRESS

$$\frac{\partial \lambda_{dip}^{MZ}}{\partial T} = \left[\frac{1}{\Delta n_{eff}}\frac{\partial \Delta n_{eff}}{\partial T} + \frac{1}{L}\frac{\partial L}{\partial T}\right]\lambda_{dip}^{MZ} \tag{10}$$

$$\frac{\partial \lambda_{dip}^{MZ}}{\partial \varepsilon} = \left[\frac{n_1 p_e}{\Delta n_{eff}} + 1\right]\lambda_{dip}^{MZ} \tag{11}$$

where $\varepsilon = \partial L/L$, $\partial n/n = -p_e\varepsilon$, $\partial t/t = -\nu\varepsilon$. p_e is the strain-optic coefficient, ν is the Poisson ratio. For silica material $p_e = 0.22$, $\nu = 0.16$. Assuming the thermal expansion coefficient (TEC) and the thermo-optic coefficient (TOC) of silica material are 5×10^{-7}/°C and 8.6×10^{-6}/°C respectively [20], the calculated temperature and strain sensitivities for ARROW dips at 1580 nm are 17.87 pm/°C and −0.92 pm/με respectively, which matches well with the previous report [38]. For MZI dips, the sensitivities are calculated to be 30.2 pm/°C and 0.36 pm/με, respectively. Note that both ARROW and MZI dips shift to a longer wavelength as temperature increases, but they move in the opposite direction when strain is applied. To verify the strain sensitivity of the MZI dips, strain measurement was performed on the S-707 sensor immersed in water to eliminate the influence from ARROW dips as shown in Fig. 10. The measured strain sensitivity of dip 1577.3 nm (0.4 pm/με) is very close to the theoretical value.

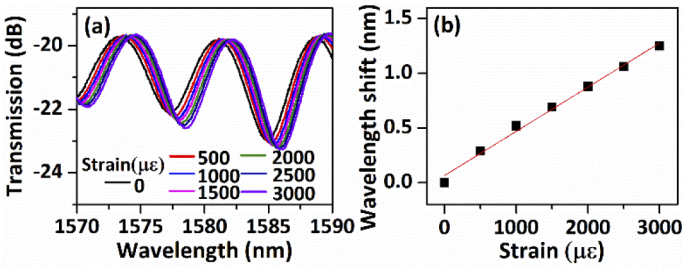

Fig. 10. Measured transmission spectra of S-707 in water under various strains and (b) the corresponding wavelength shifts. The red line in (b) is the linear fitting of the measured data.

In this work, multiple modes are involved in coupling to produce the final transmission spectrum, resulting in the superposition of multiple ARROW and MZI dips. The dips which are not sensitive to strain are most probably observed at the location where a double phase condition (destructive condition of MZI and resonant condition of ARROW) is satisfied, multiple ARROW dips and MZI dips are overlapped, resulting in a formation of a new dip with an increased strength. When an external strain is applied to the fiber structure, the strength of such a new overlapped dip may decrease (the overlap between the ARROW and MZI dips decreases) or increase after a certain value (another ARROW or MZI dip joins in). Alternatively the new overlapped dip may gradually split into two or more separate dips depending on the constituent dips' sensitivities to the corresponding parameter and on the degree of their spectral overlap. Evidence could be found in Fig. 5 and 6 where dip 2 is separating from one strong dip into two or more smaller dips while multiple smaller dips coalesce into one strong dip (dip 2') when strain is increased. The sensitivities of the overlapped dips are influenced by the sensitivities of their constituent dips. This explains why it is observed that the ARROW dips have a higher sensitivity to temperature (than theoretically calculated value) close to that of the MZI dips. Since ARROW dips and MZI dips undergo spectral shifts in opposite directions with an increase in strain, therefore the overlapped dips have much lower sensitivity compared to each single dip. It is noted that dips produced by ARROW are removed when they are totally covered in water, in real application, the sensor head cannot be fixed with glue, However since the proposed sensor structure has a very compact length in micrometers, so glue fixing on the SMFs close to the sensor head is good enough. In addition, due to its very compact size and symmetric configuration, the proposed HCF structure shows very low cross sensitivities to curvature and twist.

Optics EXPRESS

Table 2 compares our measured sensitivities with other fiber structures reported in literature. It is evident that the proposed SACHCF structure based temperature sensor shows a cross sensitivity to strain and curvature which is one to two orders of magnitude lower than sensors reported previously.

4. Conclusion

In conclusion, a high sensitivity temperature sensor with low cross-sensitivities to strain, curvature and twist is proposed based on a SACHCF structure. The light guiding principles in such an SACHCF structure are discussed and it is demonstrated that both ARROW and MZI guiding mechanisms are excited in the SACHCF structure. When a double phase condition (destructive condition of MZI and resonant condition of ARROW) is satisfied, the proposed sensor structure shows excellent temperature sensitivity of ~31.6 pm/°C but an ultra-low cross sensitivity of −0.00032 °C/με, 0.58 °C/m^{-1} and 0.71 °C/(rad/m) to strain, curvature and twist, respectively. The cross sensitivities to strain, curvature and twist which are one to two orders of magnitude lower compared to previously reported fiber optic temperature sensors. The sensor is microsized and ease of fabrication, it shows great potential for temperature measurement in complex real environments where multiple parameters are frequently encountered.

Funding. Guangdong Basic and Applied Basic Research Foundation (2019A1515110320); Shenzhen Fundamental Research Program (JCYJ20190808140805488, JCYJ20190808173401660, JCYJ20190808173619062); National Natural Science Foundation of China (11874332); National Key Scientific Instrument and Equipment Development Projects of China (61727816); Department of Agriculture, Food and the Marine, Ireland (17F284).

Disclosures. The authors declare no conflicts of interest.

Data Availability. Data underlying the results presented in this paper are not publicly available at this time but maybe obtained from the authors upon reasonable request.

References

1. R. Bogue, "Fibre optic sensors: a review of today's applications," Sens. Rev. **31**(4), 304–309 (2011).
2. D. Liu, Q. Wu, W. Han, F. Wei, F. Z. Ling, R. Kumar, A. Mallik, K. Tian, C. Shen, G. Farrell, Y. Semenova, and P. Wang, "Strain independent twist sensor based on uneven platinum coated hollow core fiber structure," Opt. Express **27**(14), 19726–19736 (2019).
3. C. Liu, Y. Jiang, B. Du, T. Wang, D. Feng, B. Jiang, and D. Yang, "Strain-insensitive twist and temperature sensor based on seven-core fiber," Sens. Actuators, A **290**, 172–176 (2019).
4. J. Wo, Q. Sun, H. Liu, X. Li, J. Zhang, D. Liu, and P. P. Shum, "Sensitivity-enhanced fiber optic temperature sensor with strain response suppression," Opt. Fiber Technol. **19**(4), 289–292 (2013).
5. Z. Cao, Z. Zhang, X. Ji, T. Shui, R. Wang, C. Yin, S. Zhen, L. Lu, and B. Yu, "Strain-insensitive and high temperature fiber sensor based on a Mach-Zehnder modal interferometer," Opt. Fiber Technol. **20**(1), 24–27 (2014).
6. Y. Zhang, Y. Yu, C. Du, S. Ruan, X. Chen, Q. Huang, and W. Zhou, "Strain-independent high-temperature sensor with a suspended-core fiber based Mach–Zehnder interferometer," Opt. Fiber Technol. **29**, 6–12 (2016).
7. S. M. Nalawade and H. V. Thakur, "Photonic crystal fiber strain-independent temperature sensing based on modal interferometer," IEEE Photonics Technol. Lett. **23**(21), 1600–1602 (2011).
8. F. Wei, D. Liu, A. K. Mallik, G. Farrell, Q. Wu, G.-D. Peng, and Y. Semenova, "Temperature-compensated magnetic field sensing with a dual-ring structure consisting of microfiber coupler-Sagnac loop and fiber Bragg grating-assisted resonant cavity," Appl. Opt. **58**(9), 2334–2339 (2019).
9. C. Lang, Y. Liu, K. Cao, and S. Qu, "Temperature-insensitive optical fiber strain sensor with ultra-low detection limit based on capillary-taper temperature compensation structure," Opt. Express **26**(1), 477–487 (2018).
10. Y. Liu, X. Liu, T. Zhang, and W. Zhang, "Integrated FPI-FBG composite all-fiber sensor for simultaneous measurement of liquid refractive index and temperature," Opt. Lasers Eng. **111**, 167–171 (2018).
11. J.-Y. Huang, J. V. Roosbroeck, J. Vlekken, A. B. Martinez, T. Geernaert, F. Berghmans, B. V. Hoe, E. Lindner, and C. Caucheteur, "FBGs written in specialty fiber for high pressure/high temperature measurement," Opt. Express **25**(15), 17936–17947 (2017).
12. T. Paixao, F. Araújo, and P. Antunes, "Highly sensitive fiber optic temperature and strain sensor based on an intrinsic Fabry–Perot interferometer fabricated by a femtosecond laser," Opt. Lett. **44**(19), 4833–4836 (2019).
13. Z. Zhang, J. He, B. Du, F. Zhang, K. Guo, and Y. Wang, "Measurement of high pressure and high temperature using a dual-cavity Fabry–Perot interferometer created in cascade hollow-core fibers," Opt. Lett. **43**(24), 6009–6012 (2018).
14. H. He, L. Shao, H. Qian, X. Zhang, J. Liang, B. Luo, W. Pan, and L. Yan, "Novel birefringence interrogation for Sagnac loop interferometer sensor with unlimited linear measurement range," Opt. Express **25**(6), 6832–6839 (2017).

Optics EXPRESS

15. J. Zhao, Y. Zhao, L. Bai, and Y. Zhang, "Sagnac Interferometer Temperature Sensor Based on Microstructured Optical Fiber Filled with Glycerin," Sens. Actuators, A **314**, 112245 (2020).
16. Z. Ou, Y. Yu, P. Yan, J. Wang, Q. Huang, X. Chen, C. Du, and H. Wei, "Ambient refractive index-independent bending vector sensor based on seven-core photonic crystal fiber using lateral offset splicing," Opt. Express **21**(20), 23812–23821 (2013).
17. R. Wang, J. Zhang, Y. Weng, Q. Rong, Y. Ma, Z. Feng, M. Hu, and X. Qiao, "Highly Sensitive Curvature Sensor Using an In-Fiber Mach-Zehnder Interferometer," IEEE Sens. J. **13**(5), 1766–1770 (2013).
18. S. Zhang, W. Zhang, S. Gao, P. Geng, and X. Xue, "Fiber-optic bending vector sensor based on Mach-Zehnder interferometer exploiting lateral-offset and up-taper," Opt. Lett. **37**(21), 4480–4482 (2012).
19. H. Gong, H. Song, X. Li, J. Wang, and X. Dong, "An optical fiber curvature sensor based on photonic crystal fiber modal interferometer," Sens. Actuators, A **195**, 139–141 (2013).
20. D. Liu, Q. Wu, C. Mei, J. Yuan, X. Xin, A. K. Mallik, F. Wei, W. Han, R. Kumar, C. Yu, S. Wan, X. He, B. Liu, G.-D. Peng, Y. Semenova, and G. Farrell, "Hollow Core Fiber Based Interferometer for High Temperature (1000 °C) Measurement," J. Lightwave Technol. **36**(9), 1583–1590 (2018).
21. N. Cai, L. Xia, and Y. Wu, "Multiplexing of anti-resonant reflecting optical waveguides for temperature sensing based on quartz capillary," Opt. Express **26**(25), 33501–33509 (2018).
22. Y. Zhao, L. Cai, and X. G. Li, "In-fiber modal interferometer for simultaneous measurement of curvature and temperature based on hollow core fiber," Opt. Laser Technol. **92**, 138–141 (2017).
23. D. Liu, R. Kumar, F. Wei, W. Han, A. K. Mallik, J. Yuan, C. Yu, Z. Kang, F. Li, Z. Liu, H.-Y. Tam, G. Farrell, Y. Semenova, and Q. Wu, "Highly sensitive twist sensor based on partially silver coated hollow core fiber structure," J. Lightwave Technol. **36**(17), 3672–3677 (2018).
24. H. Gao, Y. Jiang, L. Zhang, Y. Cui, Y. Jiang, J. Jia, and L. Jiang, "Antiresonant mechanism based self-temperature-calibrated fiber optic Fabry–Perot gas pressure sensors," Opt. Express **27**(16), 22181–22189 (2019).
25. W. Ni, P. Lu, J. Zhang, C. Yang, X. Fu, Y. Sun, H. Liao, and D. Liu, "Single hole twin eccentric core fiber sensor based on anti-resonant effect combined with inline Mach-Zehnder interferometer," Opt. Express **25**(11), 12372–12380 (2017).
26. G. Zuo, W. Li, Z. Yang, S. Li, R. Qi, Y. Huang, and L. Xia, "Double Phase Matching in MZI With Antiresonant Effect for Optical Fiber Sensor Application," J. Lightwave Technol. **39**(2), 660–666 (2021).
27. H. Cheng, S. Wu, Q. Wang, S. Wang, and P. Lu, "In-Line Hybrid Fiber Sensor for Curvature and Temperature Measurement," IEEE Photonics J. **11**(6), 1–11 (2019).
28. W. Sun, X. Zhang, Y. Yu, L. Yang, F. Hou, Y. Yang, and T. Wang, "Comparative Study on Transmission Mechanisms in a SMF-Capillary-SMF Structure," J. Lightwave Technol. **38**(15), 4075–4085 (2020).
29. Y. Zhao, L. Cai, and X. Li, "Temperature-insensitive optical fiber curvature sensor based on SMF-MMF-TCSMF-MMF-SMF structure," IEEE Trans. Instrum. Meas. **66**(1), 141–147 (2017).
30. N. M. Litchinitser, A. K. Abeeluck, C. Headley, and B. J. Eggleton, "Antiresonant reflecting photonic crystal optical waveguides," Opt. Lett. **27**(18), 1592–1594 (2002).
31. Y. Jung, S. Lee, B. H. Lee, and K. Oh, "Ultracompact in-line broadband Mach-Zehnder interferometer using a composite leaky hollow-optical-fiber waveguide," Opt. Lett. **33**(24), 2934–2936 (2008).
32. B. H. Lee and J. Nishii, "Dependence of fringe spacing on the grating separation in a long-period fiber grating pair," Appl. Opt. **38**(16), 3450–3459 (1999).
33. D. Liu, F. Ling, R. Kumar, A. K. Mallik, K. Tian, C. Shen, G. Farrell, Y. Semenova, Q. Wu, and P. Wang, "Sub-micrometer resolution liquid level sensor based on a hollow core fiber structure," Opt. Lett. **44**(8), 2125–2128 (2019).
34. D. Liu, W. Li, Q. Wu, H. Zhao, F. Ling, K. Tian, C. Shen, F. Wei, W. Han, G. Farrell, Y. Semenova, and P. Wang, "Negative Curvature Hollow Core Fiber Based All-Fiber Interferometer and Its Sensing Applications to Temperature and Strain," Sensors **20**(17), 4763 (2020).
35. R. Gao, Y. Jiang, and Y. Zhao, "Magnetic field sensor based on antiresonant reflecting guidance in the magnetic gel-coated hollow core fiber," Opt. Lett. **39**(21), 6293–6296 (2014).
36. M. Huang, C. Yang, B. Sun, Z. Zhang, and L. Zhang, "Ultrasensitive sensing in air based on graphene-coated hollow core fibers," Opt. Express **26**(3), 3098–3107 (2018).
37. A. Othonos, "Fiber Bragg gratings," Rev. Sci. Instrum. **68**(12), 4309–4341 (1997).
38. M. Hou, J. He, X. Xu, Z. Li, Z. Zhang, K. Guo, S. Ju, and Y. Wang, "Antiresonant Reflecting Guidance and Mach-Zender Interference in Cascaded Hollow-Core Fibers for Multi-Parameter Sensing," Sensors **18**(12), 4140 (2018).
39. Q. Wu, Y. Semenova, P. Wang, and G. Farrell, "Fibre heterostructure for simultaneous strain and temperature measurement," Electron. Lett. **47**(12), 713–714 (2011).
40. Y. Gong, T. Zhao, Y.-J. Rao, and Y. Wu, "All-fiber curvature sensor based on multimode interference," IEEE Photonics Technol. Lett. **23**(11), 679–681 (2011).
41. A. Zhou, B. Qin, Z. Zhu, Y. Zhang, Z. Liu, J. Yang, and L. Yuan, "Hybrid structured fiber-optic Fabry-Perot interferometer for simultaneous measurement of strain and temperature," Opt. Lett. **39**(18), 5267–5270 (2014).
42. Z. Ding and Z. Tan, "Strain and temperature discrimination based on a Sagnac interferometer with three sections of high birefringence fibers," J. Opt. Soc. Am. B **37**(2), 440–444 (2020).